Nonlinear Analytical Analysis of External Rotor Permanent Magnet Synchronous Motor

Zhaokai Li, Xiaoyan Huang, Zhuo Chen, Tingna Shi, and Yan Yan

College of Electrical Engineering, Zhejiang University, Hangzhou 310027, China

This article proposed a nonlinear analytical model (NAM) for external rotor permanent magnet synchronous motor (ER-PMSM) considering both rotor and stator saturation. The improved magnetic equivalent circuit (IMEC) is introduced to accurately describe the saturation effect of rotor and stator. The air gap reluctance is replaced by magnetic flux source, and, therefore, the size of IMEC can be reduced while keeping high accuracy. For the air gap field calculation, the analytical solution will be obtained based on the modified boundary condition from the IMEC. The complex permeance function is extended to represent the slotting effect of ER-PMSM. Hence, the NAM will be numerically solved from the combination of IMEC and analytical air gap solution. Both finite-element analysis (FEA) and experiment demonstrate that the proposed model has high accuracy and requires little time.

Index Terms— **Electromagnetic performance, equivalent magnetic circuit, nonlinear analytical model (NAM), stator and rotor saturation.**

I. Introduction

THE external rotor permanent magnet synchronous motor (ER-PMSM) has great advantage in high torque density and high efficiency. The analytical analysis for ER-PMSM is similar to that of interior rotor permanent magnet synchronous motor (IR-PMSM), since most analytical models assume that the iron permeability is infinite [1], [2]. Nevertheless, ER-PMSM usually has saturated rotor while IR-PMSM has unsaturated rotor. Hence, rotor saturation should be paid great attention to for the analytical model of ER-PMSM compared to that of IR-PMSM.

In [1], the analytical air gap solution combined with complex permeance model (CPM) was introduced to calculate the no-load field of ER-PMSM while in [2], the subdomain technique was used for predicting the electromagnetic performance of ER-PMSM. Shen and Zhu [3] investigated the optimal split ratio of ER-PMSM using a simple analytical formula. However, these models neglect the iron saturation. For the analytical models of IR-PMSM, the CPM combined with magnetic circuit was proposed to account for stator saturation [4]. Besides, the subdomain and magnetic circuit hybrid model was introduced to calculate the saturated IR-PMSM with higher accuracy [5]. However, these methods are only suitable for IR-PMSM due to the neglecting of the rotor saturation.

This article proposed a nonlinear analytical model (NAM) to calculate the magnetic field of the whole ER-PMSM considering both rotor and stator saturation. In the proposed model, the improved magnetic equivalent circuit (IMEC) was introduced to simplify the modeling of air gap region. The magnetic flux source was used to represent influence of air gap field on the magnetic potential distribution in the rotor and stator according to the IMEC. Then the modified boundary condition will be obtained from IMEC, from which the analytical air gap field of ER-PMSM is derived. Hence, the magnetic potential solution of IMEC can be numerically obtained. The NAM achieves high accuracy and reduces much computation, which is validated by finite-element analysis (FEA) and experimental results.

Manuscript received November 12, 2020; revised March 7, 2021; accepted March 15, 2021. Date of publication March 17, 2021; date of current version May 17, 2021. Corresponding author: X. Huang (e-mail: xiaoyanhuang@zju.edu.cn).

Color versions of one or more figures in this article are available at https://doi.org/10.1109/TMAG.2021.3066687.

Digital Object Identifier 10.1109/TMAG.2021.3066687

II. Nonlinear Analytical Model

In the proposed NAM, the stator and rotor are represented by the IMEC. The magnetic flux source in the IMEC is obtained from the analytical air gap field with modified boundary condition. Since the air gap magnetic reluctance is replaced by the flux source in the IMEC, the numerical solving process of NAM consumes less time. In the air gap region, the modified boundary condition is determined by the magnetic potential drop of the reluctance on the rotor bore and stator outer surface of the ER-PMSM. Hence, the magnetic field of ER-PMSM is iteratively solved using the NAM.

A. IMEC for Iron

The IMEC representing the external rotor among the range of one pair pole is shown in Fig. 1. The magnetic flux source φ_{ri} is calculated by the integral of radial air gap field B_{r}

$$\phi_{\mathrm{ri}} = R_{\mathrm{r}} l_{\mathrm{ef}} \int_{\alpha_{\mathrm{ri}}-\theta_{\mathrm{r}(i-1)}/2}^{\alpha_{\mathrm{ri}}+\theta_{\mathrm{ri}}/2} B_{\mathrm{r}}(\alpha, R_{\mathrm{r}}) d\alpha \tag{1}$$

where R_{r} and l_{ef} are the radius of the rotor bore and the effective length, respectively. α_{ri} and θ_{ri} represent the center position and the interval between the center position for rotor field integral, respectively.

In Fig. 1, the iron reluctances are distributed according to the displacement of permanent magnet (PM), which means that the magnetic flux is regarded as uniform in each magnetic path of the iron reluctance. Hence, the rotor magnetic potential Ψ_{ri} is used to obtain the modified boundary condition on the rotor bore

$$\varphi(R_{\mathrm{r}}, \alpha) = \frac{\left(\Psi_{\mathrm{r}(i+1)} - \Psi_{\mathrm{ri}}\right)(\alpha - \alpha_{\mathrm{ri}})}{\theta_{\mathrm{ri}}} + \Psi_{\mathrm{ri}} \tag{2}$$

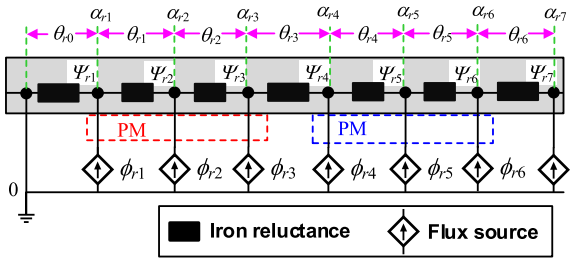

Fig. 1. Schematic view of IMEC for the rotor of ER-PMSM.

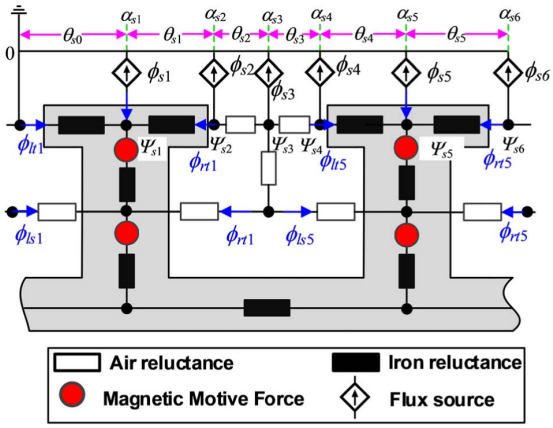

Fig. 2. Schematic view of IMEC for the stator of ER-PMSM.

where $\alpha_{\mathrm{ri}} < \alpha \le \alpha_{\mathrm{r}(i+1)}$ and Ψ_{ri} is the node magnetic potential of rotor. The solution of the rotor IMEC can be numerically calculated based on Kirchhoff's Law

$$f(\boldsymbol{\Psi}_{\mathbf{r}}) = \mathbf{A}_{\mathbf{r}}\boldsymbol{\Lambda}_{\mathbf{r}}\mathbf{A}_{\mathbf{r}}^{\mathrm{T}}\boldsymbol{\Psi}_{\mathbf{r}} - \boldsymbol{\Phi}_{\mathbf{r}} = 0 \tag{3}$$

where $\Psi_{\mathbf{r}}$ and $\Phi_{\mathbf{r}}$ are matrix form of Ψ_{ri} and φ_{ri}, respectively. $\Lambda_{\mathbf{r}}$ and $\mathbf{A}_{\mathbf{r}}$ are branch permeance matrix and node incidence matrix for rotor IMEC, respectively.

In the inner stator, the IMEC is also manipulated to represent the field distribution of stator yoke, stator tooth, and the slot, as shown in Fig. 2. Similarly, the magnetic flux source flowing into the stator φ_{sj} is calculated as

$$\phi_{\mathrm{sj}} = R_{\mathrm{s}} l_{\mathrm{ef}} \int_{\alpha_{\mathrm{sj}}-\theta_{\mathrm{s}(j-1)}/2}^{\alpha_{\mathrm{sj}}+\theta_{\mathrm{sj}}/2} B_{\mathrm{r}}(\alpha, R_{\mathrm{s}})\, d\alpha \tag{4}$$

where R_{s} is the radius of stator outer surface. α_{sj} and θ_{sj} represent the center position and the interval between the center position for stator field integral, respectively.

As the magnetic reluctances along the stator tooth shoe and slot opening are equivalent to the magnetic potential along the stator outer surface, the other modified boundary condition is obtained as

$$\varphi(R_{\mathrm{s}}, \alpha) = \frac{\left(\Psi_{\mathrm{s}(j+1)} - \Psi_{\mathrm{sj}}\right)\left(\alpha - \alpha_{\mathrm{sj}}\right)}{\theta_{\mathrm{sj}}} + \Psi_{\mathrm{sj}} \tag{5}$$

where $\alpha_{\mathrm{sj}} < \alpha \le \alpha_{\mathrm{s}(j+1)}$ and Ψ_{sj} is the node magnetic potential among tooth shoe and slot opening reluctances. According to Kirchhoff's Law, the stator IMEC can be solved using

$$f(\boldsymbol{\Psi}_{\mathbf{s}}) = \mathbf{A}_{\mathbf{s}}\boldsymbol{\Lambda}_{\mathbf{s}}\left(\mathbf{A}_{\mathbf{s}}^{\mathrm{T}}\boldsymbol{\Psi}_{\mathbf{s}} - \mathbf{E}_{\mathbf{s}}\right) - \boldsymbol{\Phi}_{\mathbf{s}} = 0 \tag{6}$$

where $\Psi_{\mathbf{s}}$ and $\Phi_{\mathbf{s}}$ are matrix form of Ψ_{sj} and ϕ_{sj}, respectively. $\Lambda_{\mathbf{s}}$ and $\mathbf{A}_{\mathbf{s}}$ are branch permeance matrix and node incidence matrix for stator IMEC, respectively.

B. Analytical Air Gap Calculation

As the iron nonlinearity and saturation effect is considered in the IMEC and the modified boundary condition is obtained, the air gap field can be analytically predicted for ER-PMSM. The total air gap field can be divided into two parts. One is the PM component obtained by solving the Poisson's equation in the PM region and Laplace's equation in the air gap region, whose boundary condition is a constant value [6]. The expression of slotless air gap field for radial and tangential PM component (B_{mr} and $B_{\mathrm{m}\alpha}$) can be found in [6]. The other is defined as IMEC-based component, which solves Laplace's equation in the whole air gap region (neglecting PM) and satisfies the modified boundary condition (2) and (5). Therefore, radial and tangential IMEC-based component of air gap field is expressed as

$$\begin{aligned} B_{\mathrm{imec\_r}} = {} & \frac{2\mu_0}{\pi}\sum_{i=1}^{6p}\sum_{v}\frac{\left(\Psi_{\mathrm{r}(i+1)} - \Psi_{\mathrm{ri}}\right)}{v\theta_{\mathrm{ri}}}\frac{1+(R_{\mathrm{s}}/r)^{2v}}{1-(R_{\mathrm{s}}/R_{\mathrm{r}})^{2v}}\frac{r^{v-1}}{R_{\mathrm{r}}^{v}} \\ & * \sin(v\theta_{\mathrm{ri}}/2)\sin\left\{v\left[\alpha - \left(\alpha_{\mathrm{ri}} + \alpha_{\mathrm{r}(i+1)}\right)/2\right]\right\} \\ & + \frac{2\mu_0}{\pi}\sum_{j=1}^{4Q_{\mathrm{s}}}\sum_{v}\frac{\left(\Psi_{\mathrm{s}(j+1)} - \Psi_{\mathrm{sj}}\right)}{v\theta_{\mathrm{sj}}}\frac{1+(R_{\mathrm{r}}/r)^{2v}}{1-(R_{\mathrm{r}}/R_{\mathrm{s}})^{2v}}\frac{r^{v-1}}{R_{\mathrm{s}}^{v}} \\ & * \sin\left(v\theta_{\mathrm{sj}}/2\right)\sin\left\{v\left[\alpha - \left(\alpha_{\mathrm{sj}} + \alpha_{\mathrm{s}(j+1)}\right)/2\right]\right\} \end{aligned} \tag{7}$$

$$\begin{aligned} B_{\mathrm{imec}\_\alpha} = {} & \frac{2\mu_0}{\pi}\sum_{i=1}^{6p}\sum_{v}\frac{\left(\Psi_{\mathrm{r}(i+1)} - \Psi_{\mathrm{ri}}\right)}{v\theta_{\mathrm{ri}}}\frac{1-(R_{\mathrm{s}}/r)^{2v}}{1-(R_{\mathrm{s}}/R_{\mathrm{r}})^{2v}}\frac{r^{v-1}}{R_{\mathrm{r}}^{v}} \\ & * \sin(v\theta_{\mathrm{ri}}/2)\sin\left\{v\left[\alpha - \left(\alpha_{\mathrm{ri}} + \alpha_{\mathrm{r}(i+1)}\right)/2\right]\right\} \\ & + \frac{2\mu_0}{\pi}\sum_{j=1}^{4Q_{\mathrm{s}}}\sum_{v}\frac{\left(\Psi_{\mathrm{s}(j+1)} - \Psi_{\mathrm{sj}}\right)}{v\theta_{\mathrm{sj}}}\frac{1-(R_{\mathrm{r}}/r)^{2v}}{1-(R_{\mathrm{r}}/R_{\mathrm{s}})^{2v}}\frac{r^{v-1}}{R_{\mathrm{s}}^{v}} \\ & * \sin\left(v\theta_{\mathrm{sj}}/2\right)\cos\left\{v\left[\alpha - \left(\alpha_{\mathrm{sj}} + \alpha_{\mathrm{s}(j+1)}\right)/2\right]\right\}. \end{aligned} \tag{8}$$

The complex permeance function is manipulated for ER-PMSM to account for slotting effect [7]. It builds up the relationship between slotted and slotless air gap field using four transformations from slotless K domain to slotted S domain

$$T = \ln(K) \tag{9}$$

$$W = e^{-j\frac{\pi}{g'}\left[T - \ln(R_{\mathrm{s}}) - j\frac{\theta_{\mathrm{s}}}{2}\right]} \tag{10}$$

$$\begin{aligned} Z = {} & -j\frac{g'}{\pi}\left[\ln\left(\frac{(b-1)W+(b-a)+(b-1)\sqrt{W-a}\sqrt{W-b}}{(b-1)W+(b-a)+(1-b)\sqrt{W-a}\sqrt{W-b}}\right)\right. \\ & \left. - 2\frac{b-1}{\sqrt{b}}\tan^{-1}\sqrt{\frac{W-b}{b(W-a)}}\right] + \ln R_{\mathrm{s}} + j\theta_1 \end{aligned} \tag{11}$$

$$S = e^{Z} \tag{12}$$

where θ_1 is half of the tooth shoe angle and θ_{s} is the angle per slot and tooth. a, b, and g' are defined in [7]. Hence, the complex permeance function can be calculated as

$$\lambda = \frac{k}{s}\frac{\omega - 1}{\sqrt{(\omega - a)(\omega - b)}} = \lambda_a + j\lambda_b. \tag{13}$$

The total radial and tangential air gap field can be calculated as

$$B_{\mathrm{r}} = \left(B_{\mathrm{mr}} + B_{\mathrm{imec\_r}}\right)\lambda_a + \left(B_{\mathrm{m}\alpha} + B_{\mathrm{imec}\_\alpha}\right)\lambda_b \tag{14}$$

$$B_{\alpha} = \left(B_{\mathrm{m}\alpha} + B_{\mathrm{imec}\_\alpha}\right)\lambda_a - \left(B_{\mathrm{mr}} + B_{\mathrm{imec\_r}}\right)\lambda_b. \tag{15}$$

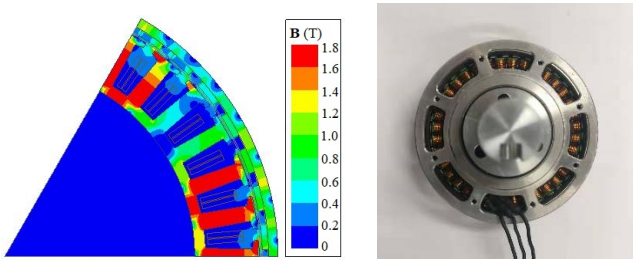

Fig. 3. 42-pole/36-slot prototype ER-PMSM in (a) FEA and (b) experiment.

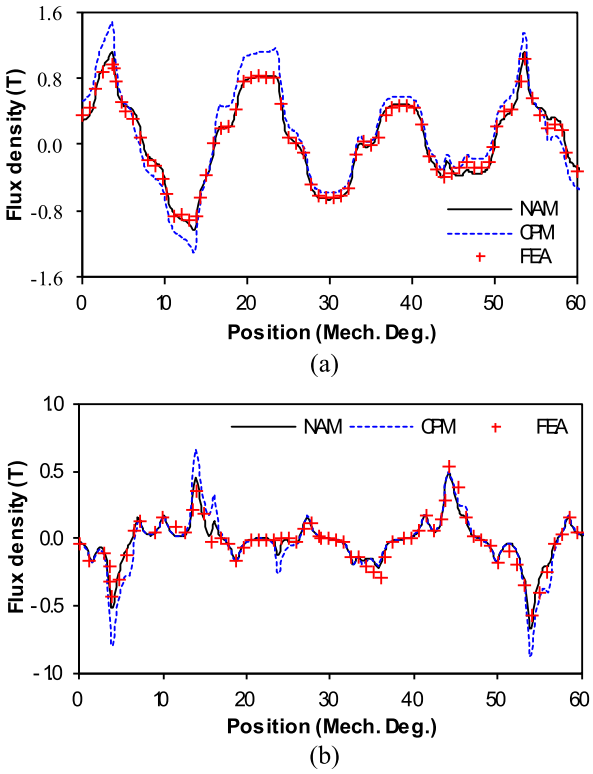

Fig. 4. (a) Radial and (b) tangential air gap field distribution along the central air gap path.

C. Calculation of ER-PMSM Performance

As the flux distribution in the IMEC is obtained, the flux linkage of ER-PMSM for each phase ψ_{ABC} is calculated as

$$\psi_{\mathrm{ABC}} = N_c \sum_{k=1,5,\ldots}^{\tau} [\varphi_{\mathrm{sk}} + \varphi_{\mathrm{ltk}} + \varphi_{\mathrm{lsk}} + \varphi_{\mathrm{rtk}} + \varphi_{\mathrm{rsk}}] \quad (16)$$

where φ_{ltk}, φ_{lsk}, φ_{rtk}, and φ_{rsk} are the tooth tip and slot leakage flux on the left and right sides of each tooth (see Fig. 2). Hence, the back electromotive force (EMF) is expressed as

$$E_{\mathrm{ABC}} = -\frac{d\psi_{\mathrm{ABC}}}{dt}. \quad (17)$$

The electromagnetic torque is calculated using Maxwell tensor theory [1]

$$T_e = \frac{1}{\mu_0} l_{\mathrm{ef}} r_0^2 \int_0^{2\pi} B_{\mathrm{r}}(\alpha, r_0) B_{\alpha}(\alpha, r_0) d\alpha \quad (18)$$

where r_0 is the radius of a closed loop path in the air gap.

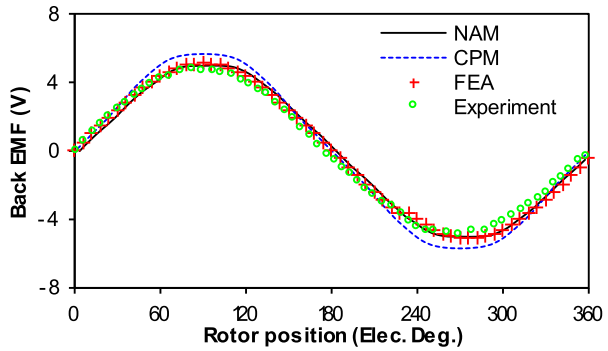

Fig. 5. Measured and calculated back EMF waveform of phase A at no-load condition.

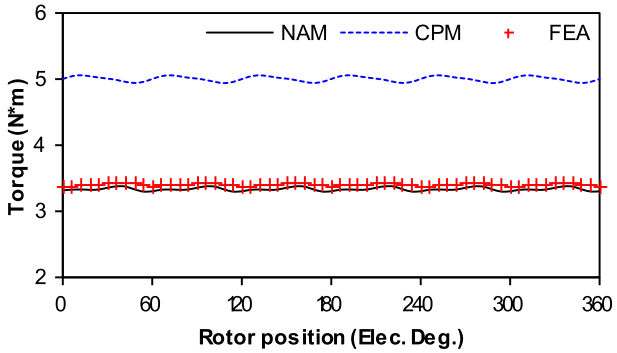

Fig. 6. Comparison of torque waveform for ER-PMSM at rated load ($I_{\mathrm{A}} = 40$ A).

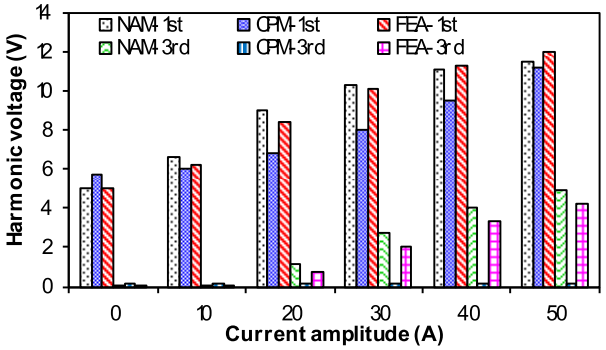

Fig. 7. Comparison of first-order and third-order harmonic induced voltage for ER-PMSM at different load.

III. FEA and Experimental Validation

An ER-PMSM with double-layer concentrated winding is analyzed using Ansys Maxwell and then it is manufactured to validate the proposed model, as shown in Fig. 3. The main parameters are given in Table I. The small permeability of rotor iron will make the rotor saturation severe, so that the difference between the NAM and CPM becomes significant.

Fig. 4 illustrates that the air gap field prediction at rated load is accurate using NAM but exhibits huge errors using CPM. For the back EMF calculation, NAM achieves excellent accuracy compared with FEA and experiment, but CPM still overestimates it, as shown in Fig. 5. Besides, NAM gives a similar waveform of electromagnetic torque compared to that of FEA, but the error of CPM can reach to nearly 47%, as shown in Fig. 6.

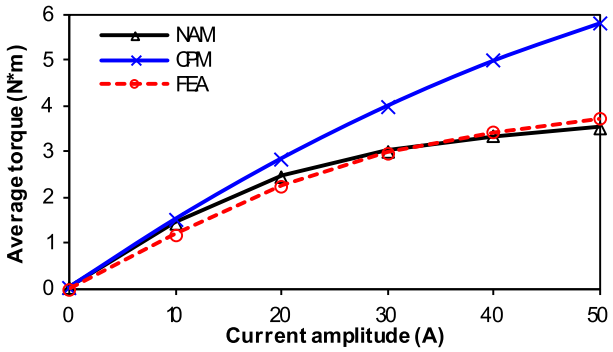

Fig. 8. Comparison of average torque for ER-PMSM at different loads.

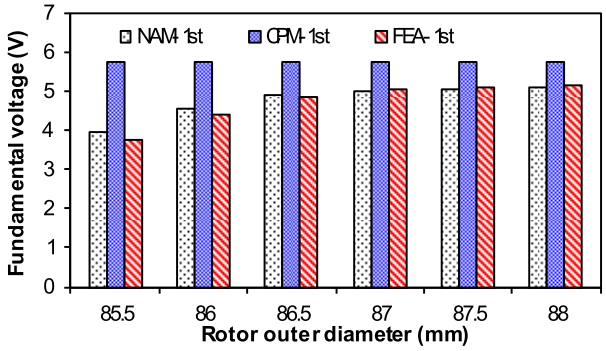

Fig. 9. Influence of rotor outer diameter on the back EMF at no-load condition.

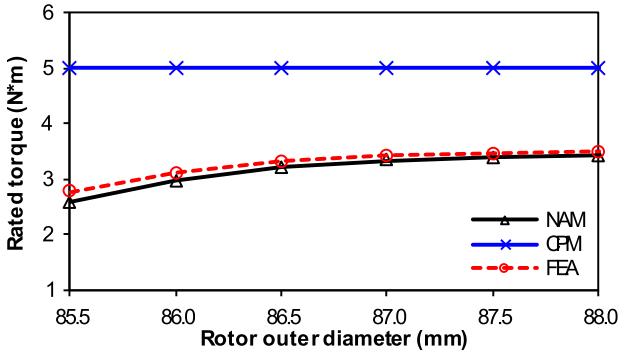

Fig. 10. Influence of rotor outer diameter on the rated torque ($I_A = 40$ A).

The nonlinearity of ER-PMSM will greatly be affected by load condition. Hence, the average torque and induced voltage predicted using NAM, CPM, and FEA are compared under different input current, as shown in Figs. 7 and 8. NAM can accurately show motor saturation level under all circumstances. For CPM, as current grows, the voltage error of firstorder harmonic varies in a certain range while the error of thirdorder induced voltage significantly increases. CPM shows low accuracy for predicting total induced voltage.

As the rotor saturation is special to ER-PMSM, the rotor outer diameter is adjusted while other parameters are kept unchanged to verify the accuracy of NAM at different saturation levels. Figs. 9 and 10 show the NAM predictions of back EMF and rated torque agree well with FEA results. Besides, as rotor outer diameter increases, the rotor saturation becomes less significant, and therefore, the CPM predictions that neglect saturation effect get close to NAM calculations.

Even the NAM achieved high accuracy, and it only consumed 5.2 and 9.3 s to calculate ER-PMSM at no-load and rated-load conditions, respectively. However, it took FEA 119 and 126 s to obtain the results under the same condition. CPM only required 0.95 and 1.1 s to predict the no-load and rated-load performances of ER-PMSM, but its accuracy is low and cannot analyze the influence of rotor and stator shapes in the design of ER-PMSM due to the assumption of infinite iron permeability.

TABLE I
MAIN PARAMETERS OF ER-PMSM

	Parameter	Value	Parameter	Value
Stator	Outer diameter	81 mm	Inner diameter	60.5 mm
	Iron material	DW315		
Magnet	Material	NdFe30	Thickness	1 mm
	Remanence	1.1 T	Relative permeability	1.04
Rotor	Outer diameter	87 mm	Inner diameter	84 mm
	Iron material	AISI 420	Effective length	8 mm

IV. CONCLUSION

In this article, the NAM is proposed for accurate field prediction in the ER-PMSM accounting for both rotor and stator saturation. The air gap reluctance is replaced by magnetic flux source in the IMEC while the rotor and stator saturations are represented by the IMEC. The IMEC will give the modified boundary condition to obtain the analytical air gap field solution. The complex permeance function is used to account for slotting effect. Hence, both iron and air gap field are numerically calculated based on the NAM. The proposed model shows great accuracy and reduces the computational time, which is demonstrated by both FEA and experimental results.

ACKNOWLEDGMENT

This work was supported in part by the Key Research and Development Program of Zhejiang under Grant 2019C01075, in part by the National Natural Science Foundation of China under Grant 51922095, and in part by the Ningbo Science and Technology Innovation 2025 Major Project under Grant 2018B10001.

REFERENCES

[1] C. Ma *et al.*, "Analytical calculation of no-load magnetic field of external rotor permanent magnet brushless direct current motor used as in-wheel motor of electric vehicle," *IEEE Trans. Magn.*, vol. 54, no. 4, Apr. 2018, Art. no. 8103106.

[2] H. Moayed-Jahromi, A. Rahideh, and M. Mardaneh, "2-D analytical model for external rotor brushless PM machines," *IEEE Trans. Energy Convers.*, vol. 31, no. 3, pp. 1100–1109, Sep. 2016.

[3] Y. Shen and Z. Q. Zhu, "Analytical prediction of optimal split ratio for fractional-slot external rotor PM brushless machines," *IEEE Trans. Magn.*, vol. 47, no. 10, pp. 4187–4190, Oct. 2011.

[4] L. J. Wu, Z. Li, D. Wang, H. Yin, X. Huang, and Z. Q. Zhu, "On-load field prediction of surface-mounted PM machines considering nonlinearity based on hybrid field model," *IEEE Trans. Magn.*, vol. 55, no. 3, Mar. 2019, Art. no. 8100911.

[5] L. Wu, H. Yin, D. Wang, and Y. Fang, "On-load field prediction in SPM machines by a subdomain and magnetic circuit hybrid model," *IEEE Trans. Ind. Electron.*, vol. 67, no. 9, pp. 7190–7201, Sep. 2020.

[6] Z. Q. Zhu, D. Howe, and C. C. Chan, "Improved analytical model for predicting the magnetic field distribution in brushless permanent-magnet machines," *IEEE Trans. Magn.*, vol. 38, no. 1, pp. 229–238, Jan. 2002.

[7] D. Zarko, D. Ban, and T. A. Lipo, "Analytical calculation of magnetic field distribution in the slotted air gap of a surface permanent-magnet motor using complex relative air-gap permeance," *IEEE Trans. Magn.*, vol. 42, no. 7, pp. 1828–1837, Jul. 2006.